

1 Title: **Imaging decision-related neural cascades in the human brain**

2

3 Authors: Jordan Muraskin¹, Truman R. Brown², Jennifer M. Walz³, Bryan Conroy⁴,

4 Robin I. Goldman⁵, Paul Sajda¹

5 ¹ Department of Biomedical Engineering, Columbia University, New York, NY, USA

6 10027

7 ² Center for Biomedical Imaging, Medical University of South Carolina, Charleston, SC,

8 USA, 29425

9 ³ Florey Institute of Neuroscience and Mental Health, Melbourne, Australia

10 ⁴ Philips Research, New York, NY,

11 ⁵ Center for Healthy Minds, University of Wisconsin-Madison, Madison, WI, USA,

12 53705

13

14 Corresponding Author: Paul Sajda, psajda@columbia.edu

15

16

17

18
19
20
21
22
23
24
25
26
27
28
29
30
31
32
33
34
35
36
37
38
39
40

Abstract

Perceptual decisions depend on coordinated patterns of neural activity cascading across the brain, running in time from stimulus to response and in space from primary sensory regions to the frontal lobe. Measuring this cascade and how it flows through the brain is key to developing an understanding of how our brains function. However observing, let alone understanding, this cascade, particularly in humans, is challenging. Here, we report a significant methodological advance allowing this observation in humans at unprecedented spatiotemporal resolution. We use a novel encoding model to link simultaneously measured electroencephalography (EEG) and functional magnetic resonance imaging (fMRI) signals to infer the high-resolution spatiotemporal brain dynamics taking place during rapid visual perceptual decision-making. After demonstrating the methodology replicates past results, we show that it uncovers a previously unobserved sequential reactivation of a substantial fraction of the pre-response network whose magnitude correlates with decision confidence. Our results illustrate that a temporally coordinated and spatially distributed neural cascade underlies perceptual decision-making, with our methodology illuminating complex brain dynamics that would otherwise be unobservable using conventional fMRI or EEG separately. We expect this methodology to be useful in observing brain dynamics in a wide range of other mental processes.

Introduction

The detailed spatiotemporal brain dynamics that underlie human decision-making are difficult to measure. Invasive techniques with sufficient temporal or spatial resolution, such as depth electrodes or cortical arrays used with epilepsy patients, are only feasible in rare cases and, in addition, do not capture activity from the entire brain. In comparison, non-invasive measures such as electroencephalography (EEG) and magnetoencephalography (MEG) suffer from poor spatial resolution, and blood oxygen level dependent functional MRI (BOLD fMRI) from poor temporal resolution and indirect coupling to neural activity (e.g. fMRI)¹. In spite of this, EEG, MEG, and fMRI have been used individually to study perceptual decision-making in the human brain, although, by themselves they provide a limited view of the underlying brain dynamics².

Recently, methods enabling simultaneous acquisition of EEG and fMRI (EEG/fMRI) have led to varied analytic approaches aimed at integrating the electrophysiological and hemodynamic information contained in the joint measurements. Such approaches offer the potential to provide a comprehensive picture of global brain dynamics, and will likely offer new insights into how the brain makes rapid decisions^{3,4}. Some of the techniques that have been proposed for combining multi-modal brain signals have separately analyzed the EEG and fMRI data and subsequently juxtaposed the results^{5,6}, while others attempt for a truly integrated approach in order to fully exploit the joint information contained in the data sets⁷. In general, simultaneous EEG/fMRI and the associated analysis techniques have been used to identify neuronal sources of EEG trial-to-trial variability, linking them to cognitive processes such as attention⁸ and inhibition⁹.

Many previous studies have used known EEG markers (P1, N2, N170, P300, α -rhythm) or data driven approaches such as Independent Component Analysis (ICA) to combine EEG with fMRI data^{4,8-16}. One promising approach has been to use supervised machine-learning techniques (e.g. classifiers) to find relevant projections of the EEG data, where single-trial variability of the electrophysiological response along these projections can be correlated in the fMRI space. Goldman, et al.¹⁷, Walz, et al.¹⁸ and Fouragnan, et al.¹⁹ have demonstrated this technique on visual and auditory paradigms. This methodology has been shown to localize cortical regions that modulate with the task while preserving the temporal progression of task-relevant neural activity.

Here we combine a classification methodology with an encoding model that relates the trial-to-trial variability in the EEG to what is observed in the simultaneously acquired fMRI. Encoding models have become an important machine learning tool for analysis of neuroimaging data, specifically fMRI²⁰. In most cases encoding models have been used to learn brain activity that encodes or represents features of a stimulus, such as visual orientation energy in an image/video²¹⁻²³, acoustic spectral power in sound/speech²⁴, or visual imagery during sleep²⁵. In the method presented here, we employ an encoding model to directly relate the simultaneously collected data from the two neuroimaging modalities—instead of features derived from the stimulus, they are derived from EEG component trial-to-trial variability. Specifically, we learn an encoding in the spatially precise fMRI data from the temporally precise trial-to-trial variability of EEG activity predictive of the level of stimulus evidence. This approach leverages the fact that the level of stimulus evidence, as measured via EEG, persists across the trial^{26,27}, and

that by discriminating this information in a time-localized way, one can temporally “tag” specific cortical areas by their trial-to-trial variability.

Using our framework for learning the BOLD signal encoding of task-relevant and temporally precise EEG component variability, we unravel the cascade of activity from the representation of sensory input to decision formation, decision action, and decision monitoring. A particularly novel finding is that after the activation of decision monitoring regions (i.e. ACC), we see a reactivation of pre-response networks, where the strength of this reactivation correlates with measures of decision confidence. This specific reactivation, as well as the entire spatio-temporal cascade, is completely unobservable using conventional fMRI-only or EEG-only methodologies.

Results

In this study, we used a visual alternative forced choice (AFC) task where subjects were shown brief presentations of pictures corrupted by noise and instructed to rapidly discriminate between object categories. On any given trial, the level of noise, or stimulus evidence, was varied randomly. The task itself, as well as similar visual decision-making tasks²⁸, is believed to engage an extensive set of cortical areas in a coordinated fashion, including regions that are responsible for sensory encoding, evidence accumulation, decision formation, and response and decision monitoring. However, the dynamic interplay of these regions has never been observed in humans. Here we exploit previously reported findings regarding the sensitivity of the EEG and fMRI signals to the level of stimulus evidence during a perceptual decision-making task. Specifically, previous work has shown differential neural responses to high vs. low

stimulus evidence in trial averaged EEG event-related potentials (ERPs), where this difference persists across the trial^{26,27}. Similarly, fMRI studies have shown that for perceptual decision making tasks a number of spatially-distributed cortical areas significantly correlate with the level of stimulus evidence^{29,30}. We leverage the fact that the level of stimulus evidence is expressed temporally in the EEG and spatially in the fMRI to “tag” voxels with a time. Specifically, using a classification methodology (i.e. discriminative components) we identify temporally precise expressions of the level of stimulus evidence that then can be spatially localized through an encoding model of the fMRI BOLD data.

We collected simultaneous EEG/fMRI data from 21 subjects as they performed a 3-AFC task discriminating between faces, cars, and houses (Fig. 1A). Subjects were instructed to discriminate the object class after briefly viewing an image corrupted by varying levels of noise (Fig. 1B) and respond by pressing one of three buttons. Overall, subjects responded with accuracies of $94 \pm 5\%$ and $58 \pm 12\%$ and with response times of $634 \pm 82\text{ms}$ and $770 \pm 99\text{ms}$ for high and low stimulus evidence trials, respectively (Fig. 1 C, D). Subject accuracies and response times across stimulus types (faces, cars, houses) for low stimulus evidence trials were similar; however, for high stimulus-evidence trials subject accuracies were higher and response times were shorter for faces than for cars or houses (See Supplemental Information Fig. S1).

GLM based analysis of BOLD fMRI shows superposition of cortical areas correlated with stimulus evidence

A traditional general linear model (GLM) analysis of the fMRI (see Methods) revealed differences in BOLD activation between the two stimulus evidence conditions (Fig. 1F, SI Table 1). Brain regions showing greater BOLD activation to high vs. low stimulus evidence trials included areas associated with early visual perception and the default mode network²⁶, such as fusiform gyrus, parahippocampal gyrus, lateral occipital cortex, superior frontal gyrus, and posterior cingulate cortex. Regions with greater BOLD activation to low vs. high stimulus evidence trials included areas in the executive control and difficulty networks: such as dorsal lateral prefrontal cortex, anterior cingulate cortex, intraparietal sulcus, and insula. Overall, these GLM results for the BOLD data reproduced previous results in the literature where similar stimuli and paradigms were used²⁹ (Fig. S2A).

Extracting temporally localized EEG signatures of stimulus evidence variability

The traditional fMRI results showed multiple brain regions correlated with the difficulty, or stimulus evidence, of the trial; however, this traditional approach does not enable one to infer the relative timing of these fMRI activations. To infer timing at a scale of tens of milliseconds, we used linear classification^{31,32} of the EEG to extract trial-to-trial variability related to stimulus evidence at specified post-stimulus time points.

The basic idea is illustrated in Figure 2, where hypothetical neural activity is shown for two different regions that are constituents of the perceptual decision-making network. Averaging over trials would clearly reveal a difference in the mean neural activity between high and low stimulus evidence. However, the two regions contribute differentially to the network, with one region encoding the stimulus evidence (Region 1)

and the other integrating it over time (Region 2); both are sensitive to the level of stimulus evidence, though varyingly so at different times in the trial. By taking advantage of this sensitivity to the stimulus evidence, we can learn EEG discriminant components, i.e. spatial filters, that best classify trials at different time windows given the neural data. We used the trial-to-trial variability along these component directions as features to uniquely tag fMRI voxels with the specific time window of the component. This tagging is done by building an encoding model of the features, given the BOLD signal, details of which are described in the following section.

We constructed EEG components by learning linear classifiers at 25ms steps, starting from stimulus onset to 50ms past the average low stimulus evidence response time. We chose a time step of 25ms due to an empirical analysis showing a half width of 50ms in the temporal autocorrelation of the EEG data, though in principle this methodology allows for temporal resolution up to the EEG sampling rate. Each classifier was associated with a set of discriminant values, which can be represented as a vector y_τ ; each element of the vector is the distance of a given trial to the discrimination boundary for the classifier at time step τ (Fig. 2). This distance can be interpreted as a measure of the EEG classifier's estimate of the level of stimulus evidence for that trial^{17,18,31-34}.

Results of the EEG analysis show discriminating information for stimulus evidence spanning the trial (see Fig. 4A), beginning roughly 175ms post-stimulus to past the average response times. A dip occurs around 300ms, indicating stimulus evidence is less discriminative at this time and serves to demarcate early and late cognitive processes. The early process corresponded to the time of the D220 ERP component, which has been shown to modulate with the degree of task difficulty, whether via stimulus noise or task

demands³⁵. The later and more prolonged component is likely related to more complex cognitive and motor preparatory processes that differ between high and low stimulus evidence trials. Importantly, although the early and late EEG components were both discriminative, we found their trial-to-trial variability to be uncorrelated (Figs. 4B and S3E), indicating that while the discriminating information (level of stimulus evidence) persists across the trial, it couples differently to processes across time.

An encoding model links fMRI activations with temporally distinct EEG trial-to-trial variability

After extracting the trial-to-trial variability from the EEG discriminant components, feature vectors y_τ are collected across time steps, τ , along with a response time vector to construct a matrix Y . This matrix is the temporally precise representation of the trial-to-trial EEG variability that reflects high vs. low stimulus evidence. An encoding model is then fit, namely a model in which weights are estimated for each time-localized EEG window, to predict the trial-to-trial variability of the BOLD response for each fMRI voxel. Figure 3 shows a schematic of the encoding model framework we used and compares it to a traditional encoding model constructed by using features derived directly from the stimulus. Rather than constructing a map that directly relates each voxel to a type of stimulus feature, such as whether it encodes edges, motion or some semantic concept such as “animal”^{21-23,36-38}, our model is used to construct maps that label voxels by the time window of the variability they encode – i.e. it “tags” each voxel with a “time”, or set of times, when it encodes the variability in the given EEG discriminant component(s).

It is important to note that this approach does not attempt to improve source localization typically done for EEG/MEG studies. Our approach instead provides the temporal resolution of EEG (ms) and the spatial resolution of fMRI (mm) without the need to solve the ill-posed inverse solution and make the many associated assumptions required for reliable source-localization results³⁹.

An example of the quality of the encoding model is shown in Fig. 4C (see also Fig. S2B) where significant voxels from the encoding model are shown in yellow. Fig. 4D shows the trial-to-trial variability of BOLD signal at a specific voxel, comparing it to the variability predicted by the encoding model. Additional validity of the encoding model and single subject results are presented in the Supplemental Information (Fig. S4A/B). The encoding model was also evaluated as a decoding model (see Methods) with the BOLD activity used to predict the trial-to-trial variability in the EEG for unseen data—data on which the encoding model was not trained. Fig. 4E shows these results, expressed as the correlation between the measured and predicted EEG trial-to-trial variability across the 800ms epoch. The shape of the curve is highly consistent with that observed for the EEG data itself (comparing Fig. 4A and Fig. 4E) (additional analysis of the fidelity of the model is provided in the SI, Fig. S3).

Given the encoding model, we unwrap the BOLD activity across time by identifying weights that are consistent across subjects in space and time (see Methods). Fig. 5 shows these results for a group level analysis. We observe a progression of activity (see Movie S1), at 25ms resolution, which proceeds simultaneously down the dorsal and ventral streams of visual processing for the first 250ms. After that the cascade becomes more complex with activation in the IPS at 425ms and 750ms (see Fig. 6A), reactivation

of the SPL at 675ms and activation of ACC at 600ms along with other regions found in the traditional fMRI results. (see Fig. S5, Tables S2 and an additional analysis using dynamic causal modeling⁴⁰). The reactivation pattern is particularly significant since it would not be observable via a traditional fMRI general linear model (GLM) analysis, which integrates over time and thus superimposes these activities. For example, the changing sign of the middle temporal gyrus (MT) encoding weights in Fig. 6A manifested as no activity in the MT for the traditional fMRI GLM analysis—the change in sign canceled the effective correlation in the GLM (see Fig. 1F and Fig. S1). The areas of activation we find are consistent with previous reports in the literature for human subjects^{29,30}; however, here we are able to link activations across time in a way that was previously only possible with invasive techniques.

Cortical reactivation correlates with decision confidence

Further analysis of the spatiotemporal dynamics (see Fig. 6B), shows that the reactivation pattern in the network occurs after decision-monitoring areas become engaged (i.e. after ACC). Spontaneous reactivation, or “replay”, of neural activity in the human brain has been observed and believed to be important for memory consolidation⁴¹ and more recently has been hypothesized to play a role in perceptual decision-making by enabling the formation of decision confidence⁴². To test the hypothesis that the reactivation activity we see is in fact related to decision confidence, we used a hierarchical drift diffusion model (DDM)^{43,44} to fit the behavioral data for high and low stimulus evidence conditions (see Methods). Specifically, our model enables us to define a proxy for decision confidence based on the DDM fits to the behavior⁴⁵. Correlating the

reactivation level to this confidence proxy shows a strong and significant monotonic relationship between confidence and the level of reactivation (high stimulus evidence-slope= 0.037 ± 0.008 , $t=4.657$, $p=3.2 \times 10^{-6}$; low stimulus evidence-slope= 0.062 ± 0.008 , $t=7.754$, $p=8.88 \times 10^{-15}$), with low stimulus evidence trials reactivated more strongly than high stimulus evidence trials (difference in slopes= -0.025 ± 0.011 , $t=2.189$, $p=0.029$)(see Fig. 7 and Fig. S7). Additionally, reactivation amplitude correlates with behavioral accuracy (Fig. S8) (high stimulus evidence, slope= 0.0115 ± 0.0047 , $t=2.41$, $p=0.016$; low stimulus evidence, slope= 0.0104 ± 0.0047 , $t=2.19$, $p=0.028$).

Discussion

We have shown that linking simultaneously acquired EEG and fMRI using a novel encoding model enables imaging of high-resolution spatiotemporal dynamics that underlie rapid perceptual decision-making — decisions made in less than a second. This method, which resolves whole-brain activity with EEG-like temporal resolution, was shown to uncover reactivation processes that would otherwise be masked by the temporal averaging and slow dynamics of traditional fMRI. More broadly, our results demonstrated a general non-invasive data-driven methodology for measuring high spatiotemporal latent neural processes underlying human behavior.

This approach temporally “tags” the BOLD fMRI data by encoding the trial-to-trial variability of the temporally precise task relevant components in simultaneously acquired EEG. In effect, the EEG discrimination indexes the activity of interest at high temporal resolution, defining a feature space, and the trial-to-trial variability of these

discriminant components becomes the specific feature values used in the encoding model. For the case presented here, this variability was used to tease apart the cascade of activity modulated by stimulus evidence across the trial, and this allowed us to observe, as never seen before, the spatiotemporal brain dynamics underlying a perceptual decision.

Previous studies have sought to generalize the timing diagram of a perceptual decision through multi-unit recordings in non-human primates^{46,47} or more broadly in humans^{29,30} using fMRI. Our results confirmed the general temporal ordering of activations found previously (early visual processing, decision formation, decision monitoring). However, there was a possibility the temporal order we observed using our technique was an artifact of our methodology. To assess this possibility, we performed additional analyses using dynamic causal modeling (DCM) to further validate the temporal activation sequence (see Fig. S6) and show, using a different set of assumptions and method, that the temporal sequence we observe is highly likely under a set of alternative sequences. We found that the most likely model is the one consistent with the time course inferred from our encoding model. The DCM results provide additional evidence that the temporal profile uncovered by the encoding model is a likely temporal decomposition of the superimposed fMRI activations.

The approach we present requires that EEG and BOLD data be collected simultaneously and not in separate sessions in order to exploit the correlations in trial-to-trial variability to “tag” the BOLD data. To show the importance of collecting the data simultaneously, we ran a control analysis that randomly permuted the trials within their stimulus evidence class, thus effectively simulating an EEG and BOLD dataset collected separately. By destroying the link between the EEG and BOLD trials, the encoding

model failed to find any consistent activation (Fig. S9/10), indicating the necessity of simultaneous acquisition.

Alternative techniques for fusing simultaneous EEG-fMRI typically do not exploit EEG across the trial and instead only analyze specific ERP components or time windows of interest^{4,8,10,12-19,48,49}. Results from these techniques identify regions that modulate with the specific components, but yield limited information about the timing of other task-relevant regions seen in traditional fMRI contrasts. The methodology developed here extends the work of¹⁷ and Walz, et al.¹⁸ by combining their EEG data reduction techniques with techniques developed for encoding stimulus features onto BOLD data^{20-23,36,38}, ultimately providing a framework for labeling voxels in task-relevant fMRI contrasts with their timing information (Fig. S2C/E/F).

Clearly, other EEG components that are task-related can be isolated and could potentially be used to “tag” BOLD data. The sliding window linear classification used here acts to reduce the EEG data along a dimension that categorizes stimulus evidence; however, this could be replaced by any other data reduction technique, such as temporally windowed ICA or PCA. Variability along these component directions could then be used in the encoding model to link with the simultaneously collected BOLD data. The choice of data reduction technique (i.e. feature space) would be highly dependent on the nature of the inferences.

Our methodology enabled us to observe reactivation of the pre-response network, spatiotemporal dynamics that would be masked using traditional fMRI analysis. Interestingly, the reactivation terminated in a network that included the MFG, insula, and IPS, similar areas previously reported to be reactivated in metacognitive judgments of

confidence in perceptual decisions^{42,50,51}. Gherman and Philiastides⁵² observed this network using a multivariate single-trial EEG approach, coupled with a distributed source reconstruction technique. Fleming, et al.⁴² and Heereman, et al.⁵³ used BOLD fMRI to show that areas in this network negatively correlate with subjective certainty ratings. Unique to our findings, we saw this reactivation on a single-trial basis after engagement of the ACC, which has been shown to be involved in decision monitoring^{52,54}, and also observed the dynamic sequence leading up to this network reactivation. Our results showed that reactivation/replay occurred on a trial-to-trial basis after a decision, was stronger for difficult decisions, and correlated with decision confidence.

The encoding model we developed was able to decompose traditional fMRI activation maps into their temporal order with significant voxel overlap between the encoding model results and traditional results. The encoding model was also able to show regions that were activated at multiple time points throughout the decision, indicating temporal dynamics that were hidden previously. The regions of activation we found are consistent with earlier findings; however, the work here provided the precise temporal decomposition of these previously reported, temporally superimposed regions of activation. In general, we have shown that simultaneously acquired EEG/fMRI data enables a novel non-invasive approach to visualize high resolution spatial and temporal processing in the human brain with the potential for providing a more comprehensive understanding of the neural basis of complex behaviors.

Methods

Subjects

21 subjects (12 male, 9 female; age range 20-35 years) participated in the study. The Columbia University Institutional Review Board (IRB) approved all experiments and informed consent was obtained before the start of each experiment. All subjects had normal or corrected-to-normal vision.

Stimuli

We used a set of 30 face (from the Max Planck Institute face database), 30 car, and 30 house (obtained from the web) gray scale images (image size 512x512 pixels, 8 bits/pixel). They were all equated for spatial frequency, luminance, and contrast. The stimulus evidence (high or low) of the task was modulated by systematically modifying the salience of the image via randomization of image phase (35% (low) and 50% (high) coherence)⁵⁵.

Experimental task

The stimuli were used in an event-related three-alternative forced choice (3-AFC) visual discrimination task. On each trial, an image -- either a face, car, or house -- was presented and subjects were instructed to respond with the category of the image by pressing one of three buttons on an MR compatible button controller. Stimuli were presented to subjects using E-Prime software (Psychology Software Tools) and a VisuaStim Digital System (Resonance Technology) with 600x800 goggle display. Over four runs, a total of 720 trials were acquired (240 of each category with 120 high coherence trials) with a random inter-trial interval (ITI) sampled uniformly between 2-2.5s. Each run lasted for 560 seconds.

fMRI acquisition

Blood-oxygenation-level-dependent (BOLD) T2*-weighted functional images were acquired on a 3T Philips Achieva scanner using a gradient-echo echo-planar imaging (EPI) pulse sequence with the following parameters: Repetition time (TR) 2000ms, echo time (TE) 25ms, flip angle 90°, slice thickness 3mm, interslice gap 1mm, in-plane resolution 3x3mm, 27 slices per volume, 280 volumes. For all of the participants, we also acquired a standard T1-weighted structural MRI scan (SPGR, resolution 1x1x1mm).

EEG acquisition

We simultaneously and continuously recorded EEG using a custom-built MR-compatible EEG system^{56,57}, with differential amplifiers and bipolar EEG montage. The caps were configured with 36 Ag/AgCl electrodes including left and right mastoids, arranged as 43 bipolar pairs. Bipolar pair leads were twisted to minimize inductive pickup from the magnetic gradient pulses and subject head motion in the main magnetic field. This oversampling of electrodes ensured data from a complete set of electrodes even in instances when discarding noisy channels was necessary. To enable removal of gradient artifacts in our offline preprocessing, we synchronized the EEG with the scanner clock by sending a transistor– transistor logic pulse at the start of each image volume. All electrode impedances were kept below 20 kΩ, which included 10 kΩ resistors built into each electrode for subject safety.

Functional image pre-processing.

Image preprocessing was performed with FSL (www.fmrib.ox.ac.uk/fsl/). Functional images were spatially realigned to the middle image in the times series (motion-correction), corrected for slice time acquisition, spatially smoothed with a 6mm FWHM Gaussian kernel, and high pass filtered (100s). The structural images were segmented

(into grey matter, white matter and cerebro-spinal fluid), bias corrected and spatially normalized to the MNI template using ‘FAST’⁵⁸. Functional images were registered into MNI space using boundary based registration (BBR)⁵⁹.

EEG data preprocessing.

We performed standard EEG preprocessing offline using MATLAB (MathWorks) with the following digital Butterworth filters: 0.5 Hz high pass to remove direct current drift, 60 and 120 Hz notches to remove electrical line noise and its first harmonic, and 100 Hz low pass to remove high-frequency artifacts not associated with neurophysiological processes. These filters were applied together in the form of a zero-phase finite impulse response filter to avoid distortions caused by phase delays. We extracted stimulus-locked 1500 ms epochs (-500:1000) and subtracted the mean baseline – -200 ms to stimulus onset – from the rest of the epoch. Through visual inspection, we discarded trials containing motion and/or blink artifacts, evidenced by sudden high-amplitude deflections.

Sliding window logistic regression.

We used linear discrimination to associate each trial with the level of stimulus evidence represented in the EEG. We considered high stimulus and low stimulus evidence trials irrespective of behavioral accuracy. Regularized logistic regression was used as a classifier to find an optimal projection for discriminating between high and low stimulus evidence trials over a specific temporal window. A sweep of the regularization parameters was implemented using FaSTGLZ⁶⁰. This approach has been previously

applied to identify neural components underlying rapid perceptual decision-making

17,18,31,33,34,45,49,61

Specifically, we defined 50ms duration training windows centered at time, τ , ranging from stimulus onset to 800ms following the stimulus in 25ms steps. We used logistic regression to estimate a spatial weighting, on N EEG channels, vector (w_τ which is N x 1) that maximally discriminated between EEG sensor array signals E for each class (e.g., high vs. low stimulus evidence trials):

$$y_\tau = w_\tau^T E_\tau \quad (1)$$

In eqn. 1, E_τ is an N x p vector (N sensors per time window τ by p trials). For our experiments, the center of the window (τ) was varied across the trial in 25ms time-steps. We quantified the performance of the linear discriminator by the area under the receiver operator characteristic (ROC) curve, referred to here as AUC, using a leave-one-out procedure. We used the ROC AUC metric to characterize the discrimination performance as a function of sliding our training window (i.e., varying τ). For each subject, this produced a matrix Y where the rows corresponded to trials and the columns to training windows, i.e. Y is the combination of the calculated y_τ for each time window.

Traditional fMRI analysis.

We first ran a traditional general linear model (GLM) fMRI analysis in FSL, using event-related (high and low stimulus evidence) and response time (RT) variability regressors. The event-related regressors comprised boxcar functions with unit amplitude and onset and offset matching that of the stimuli. RT variability was modeled using the z-scored RT as the amplitude of the boxcars with onset and offset matching that of the stimulus, and these were orthogonalized to the event-related regressors.

Orthogonalization was implemented using the Gram-Schmidt procedure⁶² to decorrelate the RT regressor from all other event-related regressors. All regressors were convolved with the canonical hemodynamic response function (HRF), and temporal derivatives were included as confounds of no interest. An event-related high versus low stimulus evidence contrast was also constructed. A fixed-effects model was used to model activations across runs, and a mixed-effects approach was used to compute the contrasts across subjects. Activated regions that passed a family-wise error (FWE)⁶³ corrected cluster threshold of $p < 0.01$ at a z-score threshold of 2.57 were considered significant.

fMRI deconvolution.

Associating fMRI data to each trial is challenging for two main reasons: (a) the temporal dynamics of the hemodynamic response function (HRF) evolve over a longer time-scale than the mean ITI of the event-related design, resulting in overlapping responses between adjacent trials; and (b) the ITI was random for each trial so that the fMRI data was not acquired at a common lag relative to stimulus onset. To overcome these issues, we employed the 'least squares - separate' (LS-S) deconvolution⁶⁴ method to estimate the voxel activations for each trial. For every trial, the time series of each voxel was regressed against a "signal" regressor and a "noise" regressor. The "signal" regressor was the modeled HRF response due to that trial (a delta function centered at stimulus onset convolved with a canonical HRF), while the "noise" regressor was the modeled HRF response due to all other trials (superimposed linearly). The resulting regression coefficients of the "signal" regressor represented the estimated voxel activations due to that trial. These voxel activations were then organized into a single brain volume per trial. We extracted 58697 voxels from a common gray matter group mask at 3 mm³ spatial

resolution that excluded white matter and CSF and assembled the resulting voxel
 activations into rows of the data matrix F .

Single subject encoding model.

All encoding model analyses were performed in MATLAB. To relate the EEG data with
 the fMRI, we devised a subject-wise spatio-temporal decomposition using singular value
 decomposition (SVD). Let F be an $m \times p$ matrix denoting m -voxels and p -trials that is the
 deconvolved high and low stimulus evidence fMRI data for each trial. Let Y be the $r \times p$
 matrix denoting r -windows (33 EEG _{τ} windows and response time (RT)) and p -trials. For
 each trial, the first row of Y is the response times while subsequent rows are the y values
 at each window time. Let W be an $m \times r$ matrix that is the weights on Y that solve for F .

$$F = WY \quad (2)$$

Normally, if we solve for W using the least squares approach, we get:

$$W = (FY^T)(YY^T)^{-1} \quad (3)$$

However, each time point might be highly correlated with its neighbors, which reduces
 the stability of the least-squares regression. We can use SVD to reduce the feature space
 and improve our estimation of W (the weights on each window). Then for a leave-one-
 out cross validation, we hold out a single trial from the EEG Y matrix and the
 corresponding volume from the fMRI data F and train on the remaining trials. We
 repeated this for all trials.

$$Y^{\text{Train}} = U\Sigma V^T \quad (4)$$

Where U is an $r \times r$ orthonormal matrix, Σ is a $r \times p$ diagonal matrix and V is a $p \times p$
 orthonormal matrix. After SVD on Y^{Train} , we reduced the feature dimensions on Y^{Train} to
 retain 75% of the variance by only keeping v components. To do this, we selected the

first v rows of Σ and zeroed the other rows. We now have $\tilde{\Sigma}$ as our reduced spaced matrix. If we now recalculate our least squares solution where we have replaced Y by its reduced form $U\tilde{\Sigma}V^T$ in equation 3:

$$\hat{W} = (F^{Train}V\tilde{\Sigma}^T)(\Sigma\Sigma^T)^{-1}U^T \quad (5)$$

So for each leave one out fold, we first calculated the SVD of the training set. We then calculated the number of components to keep and then solve for \hat{W} , the weight estimate per fold. To test, we then applied the weights to the left-out test data Y^{Test} to estimate the encoded fMRI data \hat{F} for the encoding part:

$$\hat{F} = \hat{W}Y^{Test} \quad (6)$$

While for the decoding model using the left out test data F^{Test} :

$$\hat{Y} = \hat{W}^T F^{Test} (\hat{W}^T \hat{W})^+ \quad (7)$$

Here, $\hat{W}^T \hat{W}$ is not invertible, and so we used the pseudo-inverse.

At this point, we have \hat{F} , a $m \times p$ matrix with m voxels by p trials. For each voxel j , we calculated the correlation of \hat{F}_j with F_j , resulting in the matrices R^{fMRI} (Pearson Correlation Map) and P^{fMRI} (p-value map of the Pearson Correlation) that are $m \times 1$. The P^{fMRI} was then converted to a z-score map. We constructed the $m \times r$ weight matrix W by taking the average of all the trained \hat{W} matrices. To test which time windows were significant, we also calculated, R_{τ}^{EEG} , the correlation between \hat{Y}_{τ} and Y_{τ} .

Group level spatio-temporal analysis.

For group level statistics, we first analyzed the R_{τ}^{EEG} vectors across all subjects. The R_{τ}^{EEG} vectors were converted into their p-values, and for each time window (τ), used to

compute combined Stouffer p-values⁶⁵. These group level results were then false discovery rate corrected (FDR) for multiple comparisons⁶⁶. To identify group level voxels where our model predictions were significant, each subject's p-value maps for the leave-one-out correlation were converted into their respective z-values, and voxel-wise significance was calculated using threshold-free cluster enhancement (TFCE) using a non-parametric randomization procedure implemented in FSL⁶⁷. Voxels were considered significant if they passed a conservative false discovery rate threshold of $p < 0.01$.

These significant voxels were then used as a mask to temporally localize activations by computing the voxels that were consistent in their direction (positive (high stimulus evidence) or negative (low stimulus evidence)) and timing (τ window). To this end, we implemented a spatio-temporal TFCE (stTFCE) in both space (neighboring voxels) and time (neighboring time windows - response time window not included) and computed significance through a randomization procedure. 33000 permutations (1000 permutations per window) were run by randomly altering the sign of each subject and the temporal ordering of the windows, as we were testing whether the weights were consistent in sign, voxel space, and temporal window. P-values were calculated by comparing the true stTFCE value with the distribution of permuted values. Again, voxels were considered significant if they passed FDR correction at $p < 0.05$ (high stimulus evidence: FDR-Corrected $p < 0.0019$, low stimulus evidence: FDR-Corrected $p < 0.00036$). Note, that now our number of multiple comparisons was the number of voxels in the FDR-mask (20256) times the number of time windows (33). We analyzed the response time separately with a standard TFCE randomization procedure implemented in FSL (Fig. S2D).

Dynamic causal modeling.

To validate the encoding model timing, we implemented single-state linear dynamic causal modeling (DCM) using DCM10 in SPM8⁶⁸, and applied this to the BOLD data to test the hypothesis that the temporal sequence of BOLD activations we found in our EEG-fMRI encoding method was most likely, relative to other possible sequences of these same activations, given only the BOLD data. We used the results of the encoding model to select seven regions of interest that spanned the entire trial. For the first region (labeled 175 in our figures), we computed the union of activations during the 175ms and 200ms windows. Activations of the 225ms (225) and 250ms combined with 275ms (250) windows become the second and third regions. We computed the union of activations during the 325ms and 350ms windows to create the fourth (325). For the fifth region (400), we computed the union of the activations during the 400ms-450ms windows. For the sixth region (650), we computed the union of the activations during the 650ms and 675ms windows. Finally, the union of the activations during the 725-800ms windows was computed to create the seventh region (725). We removed any overlapping voxels between any of the regions and then extracted time series from individual subjects' preprocessed functional data in MNI space by estimation of the first principal component within each region.

We constructed 11 models (Figure S6) to investigate the directed connectivity of these regions and validate the temporal ordering found by the encoding model. Each model was feed-forward with first node in each model as the input region. The first model was the temporal ordering of the regions inferred from our EEG-fMRI encoding model analysis. For five of the models, we randomized the temporal ordering of the early

regions (175, 225, 250) and the late regions (325, 400, 650, 725) separately. For the other five models, we fully randomized the temporal ordering of all the regions.

We used fixed-effects Bayesian model selection (BMS) to compare these 11 models both on a single-subject level and at the group level. BMS balances model fit and complexity, thereby selecting the most generalizable model. It estimates the relative model evidence and provides a distribution of posterior probabilities for all of the models considered. We also compared families of similar models⁶⁹; the model space was divided into two families (early/late or fully randomized).

Drift Diffusion Model (DDM) and Confidence Proxy.

The DDM models decision-making in two-choice tasks. Here, we treated the decision (correct vs. incorrect) as our two choices. A drift-process accumulates evidence over time until it crosses one of two boundaries (upper or lower) and initiates the corresponding response⁶⁸. The speed with which the accumulation process approaches one of the two boundaries (a) is called drift-rate (v) and represents the relative evidence for or against a particular response. Recently, Philastides, et al.⁴⁵ showed that for conditions in which the boundary (a) does not change, a proxy for decision confidence for each trial (i) can be computed by $1 / \sqrt{RT_i - T_{non}}$.

We used Hierarchical Bayesian estimation of the Drift-Diffusion Model in Python (HDDM) to calculate the drift rate (v), decision boundary (a) and non-decision time T_{non} for each subject⁴³. Specifically, we modeled high and low stimulus evidence response time data separately. This was to ensure our confidence proxies were consistent within trial types. We included the response time and whether the subject got the trial correct.

HDDM obtains a sequence of samples (i.e., a Markov chain Monte Carlo; MCMC) from the posterior of each parameter in the DDM. In our model, we generated 5000 samples from the posteriors, the first 1000 (burn-in) samples were discarded, and the remaining samples were thinned by 5%.

After modeling the DDM process, each trial's (i) confidence proxy (CP) for each subject (j) was computed by $CP_{i,j} = 1 / \sqrt{RT_i - T_{non,j}}$ and then z-scored across trials where $T_{non,j}$ was varied for high or low stimulus evidence trials, separately. Therefore, CP was a measure of relative trial confidence within difficulty levels.

Confidence Proxy and Decision Replay.

Trial to trial reactivation amplitude was defined as $Y_{j,i}^R = W_{j,PostACC}^T F_{j,i}$ for each subject (j) and trial (i), where $W_{postACC}$ is the weight matrix from the encoding model thresholded by voxels that were significant in the group results from the 675-800ms windows. The mean of the $Y_{j,i}^R$ across time becomes a measure of “decision replay” strength for that trial (more negative y's indicate more replay activation, more positive y's indicate less replay activation). $Y_{j,i}^R$ was quintiled for high and low stimulus evidence and the average confidence proxy was calculated within each quintile (Fig. 7). A linear mixed effects model⁷⁰ was used to test if the slope of confidences across quintile grouping, $Y_{j,i}^R$, were significantly different from 0 while including stimulus evidence as a condition. Separate similar analyses with non-replay windows (175-250ms) and testing for behavioral accuracy were also performed (Fig. S7-8).

Author Contributions

Conceptualization, J.M. and P.S.; Methodology, J.M., T.R.B., J.W. B.C., R.I.G. and P.S.; Investigation, J.M.; Software, J.M., B.C.; Writing – Original Draft, J.M. and P.S.; Writing – Review & Editing, J.M., T.R.B., R.I.G., J.W., and P.S. ; Funding Acquisition, P.S. ; Resources, J.M., T.R.B., J.W. B.C., R.I.G. and P.S.; Supervision, T.R.B and P.S.

Acknowledgements

We would like to thank Jianing Shi for assistance in collecting the EEG/fMRI data. This work was funded by National Institutes of Health Grant R01-MH085092, DARPA under Contract NBCHC090029 and the Army Research Laboratory and under Cooperative Agreement Number W911NF-10-2-0022.

References

- 1 Logothetis, N. K. What we can do and what we cannot do with fMRI. *Nature* **453**, 869-878, doi:10.1038/nature06976 (2008).
- 2 Alexander, D. M., Trengove, C. & van Leeuwen, C. Donders is dead: cortical traveling waves and the limits of mental chronometry in cognitive neuroscience. *Cognitive Processing*, doi:10.1007/s10339-015-0662-4 (2015).
- 3 Jorge, J. o., van der Zwaag, W. & Figueiredo, P. c. EEG-fMRI integration for the study of human brain function. *NeuroImage* **102**, 24--34, doi:10.1016/j.neuroimage.2013.05.114 (2014).
- 4 Huster, R. J., Debener, S., Eichele, T. & Herrmann, C. S. Methods for simultaneous EEG-fMRI: an introductory review. *The Journal of neuroscience : the official journal of the Society for Neuroscience* **32**, 6053-6060, doi:10.1523/jneurosci.0447-12.2012 (2012).
- 5 Plichta, M. M. *et al.* Simultaneous EEG and fMRI Reveals a Causally Connected Subcortical-Cortical Network during Reward Anticipation. *Journal of Neuroscience* **33**, 14526-14533, doi:10.1523/jneurosci.0631-13.2013 (2013).
- 6 Yuan, H. *et al.* Negative covariation between task-related responses in alpha/beta-band activity and BOLD in human sensorimotor cortex: an EEG and fMRI study of motor imagery and movements. *NeuroImage* **49**, 2596-2606, doi:10.1016/j.neuroimage.2009.10.028 (2010).
- 7 Dahne, S. *et al.* Multivariate Machine Learning Methods for Fusing Multimodal Functional Neuroimaging Data. *Proceedings of the IEEE* **103**, 1507-1530, doi:10.1109/JPROC.2015.2425807 (2015).

619 8 Warbrick, T., Arrubla, J., Boers, F., Neuner, I. & Shah, N. J. J. J. Attention to
620 Detail: Why Considering Task Demands Is Essential for Single-Trial Analysis of
621 BOLD Correlates of the Visual P1 and N1. *Journal of cognitive neuroscience* **26**,
622 1--14, doi:10.1162/jocn (2013).

623 9 Baumeister, S. *et al.* Sequential inhibitory control processes assessed through
624 simultaneous EEG-fMRI. *NeuroImage*, doi:10.1016/j.neuroimage.2014.01.023
625 (2014).

626 10 Novitskiy, N., Ramautar, J. R. & Vanderperren, K. a. The BOLD correlates of the
627 visual P1 and N1 in single-trial analysis of simultaneous EEG-fMRI recordings
628 during a spatial detection task. *NeuroImage* **54**, 824--835,
629 doi:10.1016/j.neuroimage.2010.09.041 (2010).

630 11 Nguyen, V. T. & Cunnington, R. The superior temporal sulcus and the N170
631 during face processing: Single trial analysis of concurrent EEG-fMRI.
632 *NeuroImage*, doi:10.1016/j.neuroimage.2013.10.047 (2013).

633 12 De Martino, F. *et al.* Multimodal imaging: an evaluation of univariate and
634 multivariate methods for simultaneous EEG/fMRI. *Magnetic resonance imaging*
635 **28**, 1104-1112, doi:10.1016/j.mri.2009.12.026 (2010).

636 13 Mayhew, S. D., Ostwald, D., Porcaro, C. & Bagshaw, A. P. Spontaneous EEG
637 alpha oscillation interacts with positive and negative BOLD responses in the
638 visual-auditory cortices and default-mode network. *NeuroImage* **76**, 362-372,
639 doi:10.1016/j.neuroimage.2013.02.070 (2013).

640 14 Jann, K. *et al.* BOLD correlates of EEG alpha phase-locking and the fMRI default
641 mode network. *NeuroImage* **45**, 903-916, doi:10.1016/j.neuroimage.2009.01.001
642 (2009).

643 15 Jaspers-Fayer, F., Ertl, M., Leicht, G., Leupelt, A. & Mulert, C. Single-trial EEG-
644 fMRI coupling of the emotional auditory early posterior negativity. *NeuroImage*
645 **62**, 1807-1814, doi:10.1016/j.neuroimage.2012.05.018 (2012).

646 16 Omata, K., Hanakawa, T., Morimoto, M. & Honda, M. Spontaneous Slow
647 Fluctuation of EEG Alpha Rhythm Reflects Activity in Deep-Brain Structures: A
648 Simultaneous EEG-fMRI Study. *PloS one* **8**, e66869-e66869,
649 doi:10.1371/journal.pone.0066869 (2013).

650 17 Goldman, R. I. *et al.* Single-trial discrimination for integrating simultaneous EEG
651 and fMRI: identifying cortical areas contributing to trial-to-trial variability in the
652 auditory oddball task. *NeuroImage* **47**, 136-147,
653 doi:10.1016/j.neuroimage.2009.03.062 (2009).

654 18 Walz, J. M. *et al.* Simultaneous EEG-fMRI Reveals Temporal Evolution of
655 Coupling between Supramodal Cortical Attention Networks and the Brainstem.
656 *The Journal of neuroscience : the official journal of the Society for Neuroscience*
657 **33**, 19212-19222, doi:10.1523/jneurosci.2649-13.2013 (2013).

658 19 Fouragnan, E., Retzler, C., Mullinger, K. & Philiastides, M. G. Two
659 spatiotemporally distinct value systems shape reward-based learning in the human
660 brain. *Nature communications* **6**, 8107, doi:10.1038/ncomms9107 (2015).

661 20 Naselaris, T., Kay, K. N., Nishimoto, S. & Gallant, J. L. Encoding and decoding
662 in fMRI. *NeuroImage* **56**, 400-410, doi:10.1016/j.neuroimage.2010.07.073
663 (2011).

664 21 Hansen, K. A., Kay, K. N. & Gallant, J. L. Topographic organization in and near
665 human visual area V4. *Journal of Neuroscience* **27**, 11896--11911,
666 doi:10.1523/JNEUROSCI.2991-07.2007 (2007).

667 22 Kay, K. N., Naselaris, T., Prenger, R. J. & Gallant, J. L. Identifying natural
668 images from human brain activity. *Nature* **452**, 352--355,
669 doi:10.1038/nature06713 (2008).

670 23 Nishimoto, S. *et al.* Reconstructing visual experiences from brain activity evoked
671 by natural movies. *Current Biology* **21**, 1641--1646,
672 doi:10.1016/j.cub.2011.08.031 (2011).

673 24 Silbert, L. J., Honey, C. J., Simony, E., Poeppel, D. & Hasson, U. Coupled neural
674 systems underlie the production and comprehension of naturalistic narrative
675 speech. *Proceedings of the National Academy of Sciences* **111**, E4687--E4696,
676 doi:10.1073/pnas.1323812111 (2014).

677 25 Horikawa, T., Tamaki, M., Miyawaki, Y. & Kamitani, Y. Neural decoding of
678 visual imagery during sleep. *Science (New York, N.Y.)* **340**, 639-642,
679 doi:10.1126/science.1234330 (2013).

680 26 Philiastides, M. G., Ratcliff, R. & Sajda, P. Neural representation of task
681 difficulty and decision making during perceptual categorization: a timing
682 diagram. *The Journal of neuroscience : the official journal of the Society for*
683 *Neuroscience* **26**, 8965-8975, doi:10.1523/JNEUROSCI.1655-06.2006 (2006).

684 27 Banko, E. M., Gal, V., Kortvelyes, J., Kovacs, G. & Vidnyanszky, Z. Dissociating
685 the effect of noise on sensory processing and overall decision difficulty. *The*
686 *Journal of neuroscience : the official journal of the Society for Neuroscience* **31**,
687 2663-2674, doi:10.1523/JNEUROSCI.2725-10.2011 (2011).

688 28 Erickson, D. T. & Kayser, A. S. The neural representation of sensorimotor
689 transformations in a human perceptual decision making network. *NeuroImage*
690 **79C**, 340-350, doi:10.1016/j.neuroimage.2013.04.085 (2013).

691 29 Heekeren, H. R., Marrett, S., Bandettini, P. a. & Ungerleider, L. G. A general
692 mechanism for perceptual decision-making in the human brain. *Nature* **431**, 859-
693 862, doi:10.1038/nature02966 (2004).

694 30 Philiastides, M. G. & Sajda, P. EEG-informed fMRI reveals spatiotemporal
695 characteristics of perceptual decision making. *The Journal of neuroscience : the*
696 *official journal of the Society for Neuroscience* **27**, 13082-13091,
697 doi:10.1523/JNEUROSCI.3540-07.2007 (2007).

698 31 Parra, L. C., Spence, C. D., Gerson, A. D. & Sajda, P. Recipes for the linear
699 analysis of EEG. *NeuroImage* **28**, 326-341,
700 doi:10.1016/j.neuroimage.2005.05.032 (2005).

701 32 Sajda, P., Philiastides, M. G. & Parra, L. C. Single-trial analysis of neuroimaging
702 data: inferring neural networks underlying perceptual decision-making in the
703 human brain. *IEEE Rev Biomed Eng* **2**, 97-109,
704 doi:10.1109/RBME.2009.2034535 (2009).

705 33 Muraskin, J., Sherwin, J. & Sajda, P. Knowing when not to swing: EEG evidence
706 that enhanced perception-action coupling underlies baseball batter expertise.
707 *NeuroImage* **123**, 1-10, doi:10.1016/j.neuroimage.2015.08.028 (2015).

708 34 Sherwin, J., Muraskin, J. & Sajda, P. You Can't Think and Hit at the Same Time:
709 Neural Correlates of Baseball Pitch Classification. *Frontiers in neuroscience* **6**,
710 177, doi:10.3389/fnins.2012.00177 (2012).

711 35 Philiastides, M. G. & Sajda, P. Temporal characterization of the neural correlates
712 of perceptual decision making in the human brain. *Cereb Cortex* **16**, 509-518,
713 doi:10.1093/cercor/bhi130 (2006).

714 36 Cukur, T., Nishimoto, S., Huth, A. G. & Gallant, J. L. Attention during natural
715 vision warps semantic representation across the human brain. *Nature*
716 *neuroscience* **16**, 763-770, doi:10.1038/nn.3381 (2013).

717 37 Naselaris, T., Kay, K. N., Nishimoto, S. & Gallant, J. L. Vol. 56 400-410
718 (2011).

719 38 Stansbury, D., Naselaris, T. & Gallant, J. Natural Scene Statistics Account for the
720 Representation of Scene Categories in Human Visual Cortex. *Neuron* **79**, 1025--
721 1034, doi:10.1016/j.neuron.2013.06.034 (2013).

722 39 Wendel, K. *et al.* EEG/MEG source imaging: methods, challenges, and open
723 issues. *Computational intelligence and neuroscience*, 656092,
724 doi:10.1155/2009/656092 (2009).

725 40 Friston, K. J., Harrison, L. & Penny, W. Dynamic causal modelling. *NeuroImage*
726 **19**, 1273--1302, doi:10.1016/S1053-8119(03)00202-7 (2003).

727 41 Deuker, L. *et al.* Memory consolidation by replay of stimulus-specific neural
728 activity. *The Journal of neuroscience : the official journal of the Society for*
729 *Neuroscience* **33**, 19373-19383, doi:10.1523/JNEUROSCI.0414-13.2013 (2013).

730 42 Fleming, S. M., Huijgen, J. & Dolan, R. J. Prefrontal contributions to
731 metacognition in perceptual decision making. *The Journal of neuroscience : the*
732 *official journal of the Society for Neuroscience* **32**, 6117-6125,
733 doi:10.1523/JNEUROSCI.6489-11.2012 (2012).

734 43 Wiecki, T. V., Sofer, I. & Frank, M. J. HDDM: Hierarchical Bayesian estimation
735 of the Drift-Diffusion Model in Python. *Frontiers in neuroinformatics* **7**, 14,
736 doi:10.3389/fninf.2013.00014 (2013).

737 44 Ratcliff, R. & McKoon, G. The diffusion decision model: theory and data for two-
738 choice decision tasks. *Neural Comput* **20**, 873--922, doi:10.1162/neco.2008.12-
739 06-420 (2008).

740 45 Philiastides, M. G., Heekeren, H. R. & Sajda, P. Human Scalp Potentials Reflect a
741 Mixture of Decision-Related Signals during Perceptual Choices. *Journal of*
742 *Neuroscience* **34**, 16877--16889, doi:10.1523/JNEUROSCI.3012-14.2014 (2014).

743 46 Siegel, M., Buschman, T. J. & Miller, E. K. Cortical information flow during
744 flexible sensorimotor decisions. *Science* **348**, 1352-1355,
745 doi:10.1126/science.aab0551 (2015).

746 47 Gold, J. I. & Shadlen, M. N. The neural basis of decision making. *Annual review*
747 *of neuroscience* **30**, 535-574, doi:10.1146/annurev.neuro.29.051605.113038
748 (2007).

749 48 Warbrick, T. *et al.* Single-trial P3 amplitude and latency informed event-related
750 fMRI models yield different BOLD response patterns to a target detection task.
751 *NeuroImage* **47**, 1532-1544, doi:10.1016/j.neuroimage.2009.05.082 (2009).

752 49 Walz, J. M. *et al.* Simultaneous EEG-fMRI reveals a temporal cascade of task-
753 related and default-mode activations during a simple target detection task.
754 *NeuroImage* **102 Pt 1**, 229-239, doi:10.1016/j.neuroimage.2013.08.014 (2014).
755 50 Yeung, N. & Summerfield, C. Metacognition in human decision-making:
756 confidence and error monitoring. *Philosophical transactions of the Royal Society*
757 *of London. Series B, Biological sciences* **367**, 1310-1321,
758 doi:10.1098/rstb.2011.0416 (2012).
759 51 Steinhäuser, M. & Yeung, N. Decision processes in human performance
760 monitoring. *The Journal of neuroscience : the official journal of the Society for*
761 *Neuroscience* **30**, 15643-15653, doi:10.1523/JNEUROSCI.1899-10.2010 (2010).
762 52 Gherman, S. & Philiastides, M. G. Neural representations of confidence emerge
763 from the process of decision formation during perceptual choices. *NeuroImage*
764 **106**, 134-143, doi:10.1016/j.neuroimage.2014.11.036 (2015).
765 53 Heereman, J., Walter, H. & Heekeren, H. R. A task-independent neural
766 representation of subjective certainty in visual perception. *Front Hum Neurosci* **9**,
767 551, doi:10.3389/fnhum.2015.00551 (2015).
768 54 Botvinick, M. M., Braver, T. S., Barch, D. M., Carter, C. S. & Cohen, J. D.
769 Conflict monitoring and cognitive control. *Psychological review* **108**, 624-652
770 (2001).
771 55 Dakin, S. C., Hess, R. F., Ledgeway, T. & Achtman, R. L. What causes non-
772 monotonic tuning of fMRI response to noisy images? *Current biology : CB* **12**,
773 R476-477; author reply R478 (2002).
774 56 Sajda, P., Goldman, R. I., Dyrholm, M. & Brown, T. R. *Signal Processing and*
775 *Machine Learning for Single-trial Analysis of Simultaneously Acquired EEG and*
776 *fMRI*. (Elsevier Inc., 2010).
777 57 Sajda, P., Goldman, R. I., Philiastides, M. G., Gerson, A. D. & Brown, T. R. A
778 System for Single-trial Analysis of Simultaneously Acquired EEG and fMRI.
779 *2007 3rd International IEEE/EMBS Conference on Neural Engineering*,
780 doi:10.1109/CNE.2007.369667 (2007).
781 58 Zhang, Y., Brady, M. & Smith, S. Segmentation of brain MR images through a
782 hidden Markov random field model and the expectation-maximization algorithm.
783 *IEEE transactions on medical imaging* **20**, 45--57, doi:10.1109/42.906424 (2001).
784 59 Greve, D. N. & Fischl, B. Accurate and robust brain image alignment using
785 boundary-based registration. *NeuroImage* **48**, 63--72,
786 doi:10.1016/j.neuroimage.2009.06.060 (2009).
787 60 Conroy, B. R., Walz, J. M. & Sajda, P. Fast bootstrapping and permutation testing
788 for assessing reproducibility and interpretability of multivariate FMRI decoding
789 models. *PloS one* **8**, e79271, doi:10.1371/journal.pone.0079271 (2013).
790 61 Sherwin, J. & Sajda, P. Musical experts recruit action-related neural structures in
791 harmonic anomaly detection: evidence for embodied cognition in expertise. *Brain*
792 *and Cognition* **83**, 190-202, doi:10.1016/j.bandc.2013.07.002 (2013).
793 62 Strang, G. Introduction to Linear Algebra. *Mathematics of Computation* **18**, 510,
794 doi:10.2307/2003783 (2003).
795 63 Nichols, T. & Hayasaka, S. Controlling the familywise error rate in functional
796 neuroimaging: a comparative review. *Statistical methods in medical research* **12**,
797 419--446, doi:10.1191/0962280203sm341ra (2003).

798 64 Mumford, J. A., Turner, B. O., Ashby, F. G. & Poldrack, R. A. Deconvolving
799 BOLD activation in event-related designs for multivoxel pattern classification
800 analyses. *NeuroImage* **59**, 2636-2643, doi:10.1016/j.neuroimage.2011.08.076
801 (2012).

802 65 Darlington, R. B. & Hayes, A. F. Combining independent p values: extensions of
803 the Stouffer and binomial methods. *Psychological methods* **5**, 496-515,
804 doi:10.1037/1082-989X.5.4.496 (2000).

805 66 Benjamini, Y. & Hochberg, Y. Controlling the False Discovery Rate: A Practical
806 and Powerful Approach to Multiple Testing. *Journal of the Royal Statistical*
807 *Society. Series B (Methodological)* **57**, 289 -- 300, doi:10.2307/2346101 (1995).

808 67 Smith, S. M. & Nichols, T. E. Threshold-free cluster enhancement: addressing
809 problems of smoothing, threshold dependence and localisation in cluster
810 inference. *NeuroImage* **44**, 83-98, doi:10.1016/j.neuroimage.2008.03.061 (2009).

811 68 Stephan, K. E. *et al.* Ten simple rules for dynamic causal modeling. *NeuroImage*
812 **49**, 3099--3109, doi:10.1016/j.neuroimage.2009.11.015 (2010).

813 69 Penny, W. D. *et al.* Comparing families of dynamic causal models. *PLoS*
814 *Computational Biology* **6**, doi:10.1371/journal.pcbi.1000709 (2010).

815 70 Bates, D., Mächler, M., Bolker, B. & Walker, S. Fitting Linear Mixed-Effects
816 Models Using lme4. *2015* **67**, 48, doi:10.18637/jss.v067.i01 (2015).
817
818

Figure Captions

Figure 1. Paradigm and traditional EEG and fMRI results

A, 3-AFC task where stimulus evidence for each category is modulated by varying the phase coherence in the images. **B**, Example of face images with high stimulus evidence (high coherence: 50%) and low stimulus evidence (low coherence: 35%). **C**, Behavioral performance shows significant differences, as a function of stimulus evidence, in accuracy ($p < 10^{-12}$, paired t-test) and **D**, response time ($p < 10^{-8}$, paired t-test) across the group. **E**, Grand average stimulus-locked event related potentials (ERPs) for electrode Pz show that differences in stimulus evidence span the time from stimulus to response. **F**, fMRI analysis showing cortical areas correlated with high (red) vs. low (blue) stimulus evidence across the entire trial ($Z > 2.57$ with $p < 0.01$ Family-Wise Error cluster corrected).

Figure 2. Temporally precise trial-to-trial EEG variability tags brain regions during decision-making

A, Illustration of how trial-to-trial variability of neural activity in spatially distinct cortical areas can be used to tag brain regions. In this hypothetical example Region 1 is involved in sensory encoding while Region 2 integrates sensory evidence to form a decision (in NHP literature, Region 1 might represent MT, while Region 2 LIP). Neural activity across the trial is shown for two stimulus types, one with high sensory evidence for the choice (red curves) and one with low sensory evidence (blue curves). Also shown are two temporal windows (τ_1 and τ_2) that represent different times during the trial. **B**, Linear classifiers are trained to separate trials based on the two levels of stimulus evidence at specific temporal windows. Shown are classifiers (parameterized by weight

vectors w_1 and w_2) for two temporal windows (τ_1 and τ_2) with respect to two EEG sensors (for simplicity only two dimensions of the full $N=43$ sensor space are shown. Though the component hyperplane is optimal for the full 43 dimensions, when projected to a line in two dimensions for illustration, it may appear that the separation is sub-optimal). This yields an EEG discriminant component for each temporal window. Variability along these components serves as a unique feature vector for temporally tagging the BOLD data—e.g. variability along an EEG component trained with data from τ_1 tags BOLD voxels with time τ_1 while variability along an EEG component trained with data from τ_2 tags them with τ_2 .

Figure 3. Encoding models based on stimulus derived features versus EEG variability

A, A traditional encoding model used in fMRI analysis extracts a set of features from the stimulus that are potentially representative of low level structure and high level semantics (green box). Weights are learned to model how these stimulus features are encoded in the fMRI BOLD signal. The resulting encoding model is used to make predictions based on how well different voxels predict the features from novel stimuli. For example, one can create maps of the brain that are labeled based on the stimulus features that each voxel represents. **B**, The same encoding model concept applied to EEG variability (EEG encoding model). Instead of features being estimated from the stimulus, they are derived from EEG component trial-to-trial variability (as in Fig 2a) with each temporal window representing a different feature (green box). Weights are learned so as to model how the EEG variability at a given time window is encoded in the fMRI BOLD. As in the

traditional encoding model, predictions on novel stimuli can be done to test the model and results can be used to construct a map—in this case a map of the brain that shows the timing of the EEG component variability that each voxels represents.

Figure 4. **EEG discrimination and encoding model results**

A, Group average area under the receiver operating curve (AUC) for the sliding window logistic regression EEG discrimination analysis, comparing high versus low stimulus evidence trials; standard error across subjects is shown with shading. **B**, A single subject's discriminating y-value distributions for high (red) and low stimulus evidence (blue) trials for two EEG time points (225ms and 600ms). **C**, Significant fMRI voxels resulting from the group level analysis for the encoding model ($p < 0.01$ TFCE-False Discovery Rate (FDR) corrected). Activity is seen encompassing early visual processing regions, attention networks, and the task positive network. **D**, A random subset of 100 (50 for each stimulus evidence condition) from 700 total trials of the actual (circle) and predicted (diamond) BOLD responses from the encoding model, for an example subject at a single voxel (MNI X/Y/Zmm: -27/-54/-15, $r=0.206$, $p < 10^{-6}$). High and low stimulus evidence trials are shown separately for clarity. **E**, The averaged correlation of the predicted y-values with the true y-values across the trial duration. Blue shading represents the standard error across subjects. Grey shading indicates significant time windows ($p < 0.05$ FDR-corrected).

Figure 5. **Group-level encoding model weights results show neural activation cascade**

Subset of thresholded ($p < 0.05$ FDR-Corrected, $k=10$) group level statistical parametric maps created by stTFCE randomization procedure on the encoding model weight matrices show the progression of spatial activity across the trial. Activation can be seen early in the trial in the occipital regions while progressing more anteriorly later in the trial to executive control areas. Activations in red indicate areas where high stimulus evidence trials had larger activations than low stimulus evidence trials, and blue the inverse.

Figure 6. Spatial-temporal event-related activations show coordinated reactivations.

A, Union across time windows of significant voxels for high (red) and low (blue) stimulus evidence activations. Voxels with activations for both high and low conditions (at different time windows) are displayed in green. Also shown are the encoding model weights for specific voxels, including fusiform gyrus (FG-R):36/-51/-18, (FG-L):-42/-42/-18, superior lateral occipital cortex (sLOC):24/-63/36, superior parietal lobule (SPL):27/-51/54, anterior cingulate cortex (ACC):-6/24/30, intraparietal sulcus (IPS):-30/-60/39, middle frontal gyrus (MFG):-45/27/30, middle temporal gyrus (MT):-57/-60/0. Asterisks indicate significant windows. **B**, Sequence of significant weights showing a “replay” of the network after the onset of ACC activation (shaded ellipse). “Replay” is faster than the initial stimulus driven sequence and strongest for low evidence trials.

Figure 7. Trial-to-trial reactivation correlates with decision confidence.

Trial-to-trial reactivation amplitude ($Y_{j,i}^R$ – see Methods) of “replay” correlates with confidence proxy for both high and low stimulus evidence conditions. Error bars represent standard errors across subjects.

Figures:

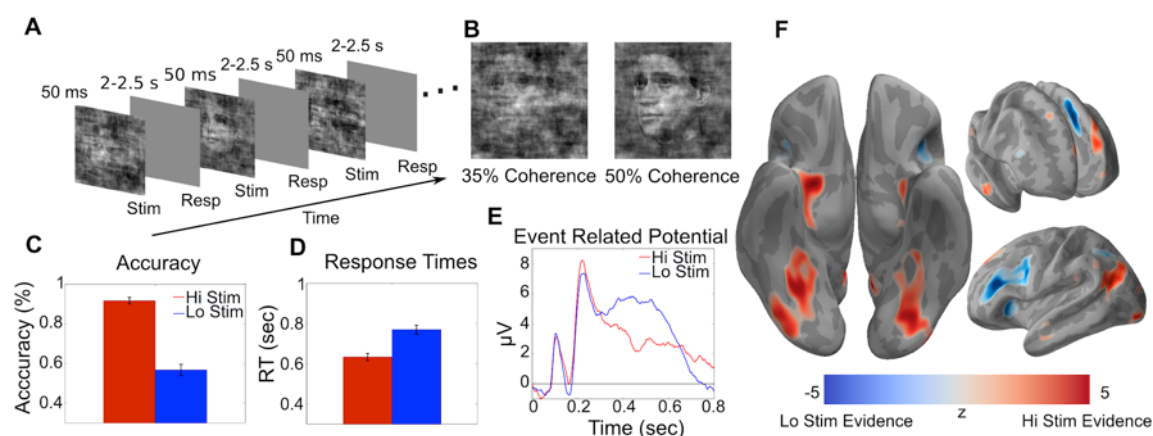


Figure 1.

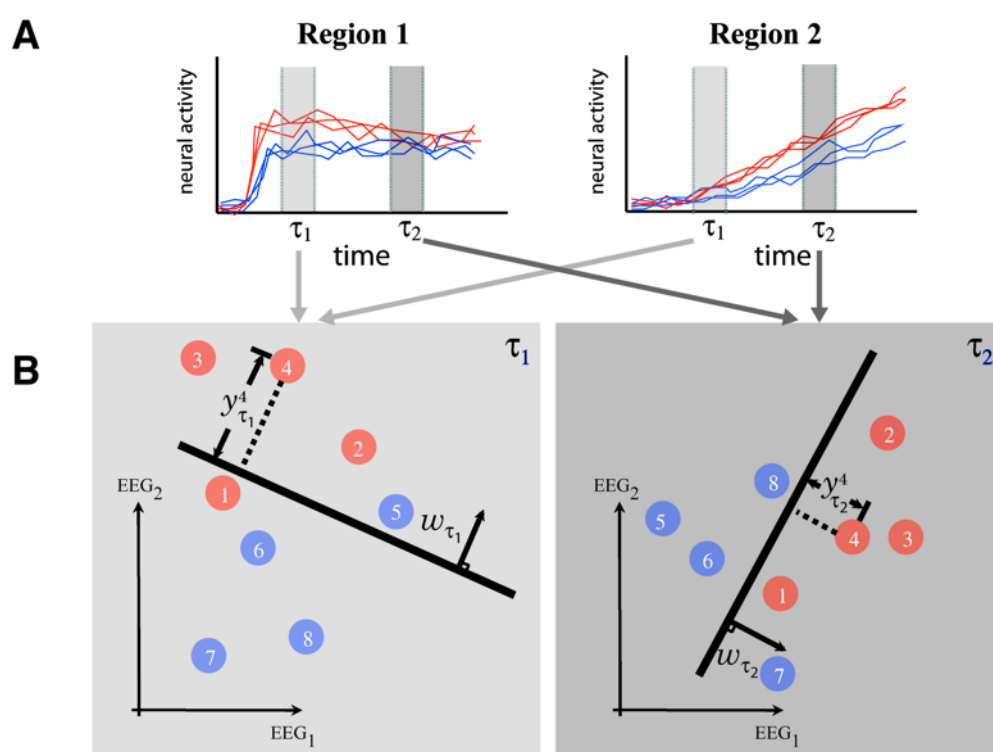


Figure 2.

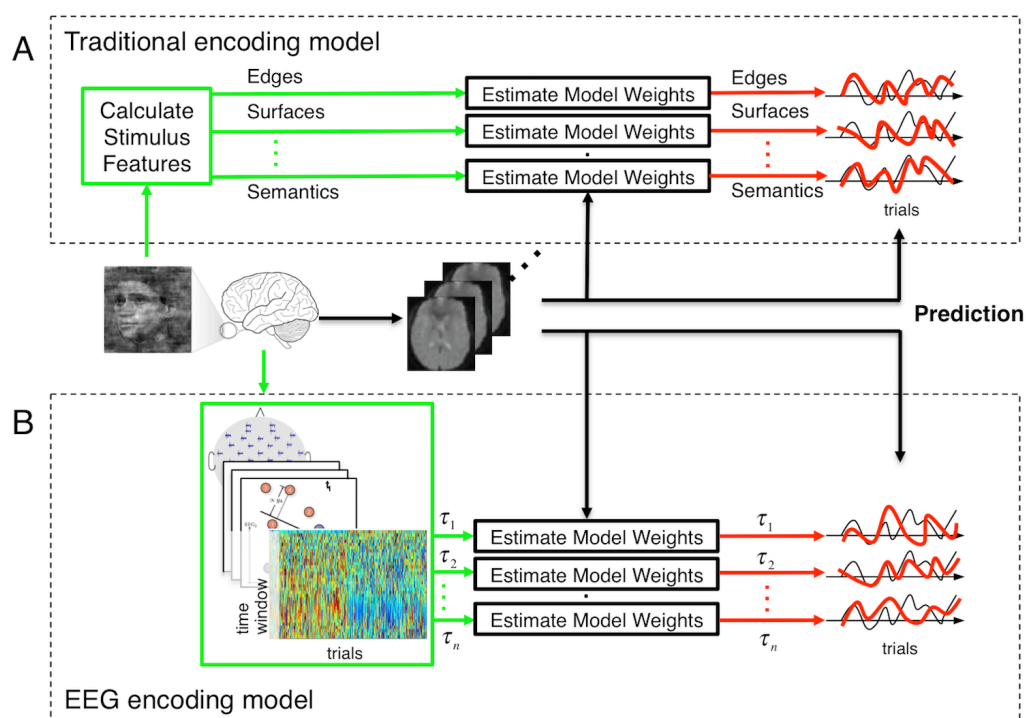


Figure 3.

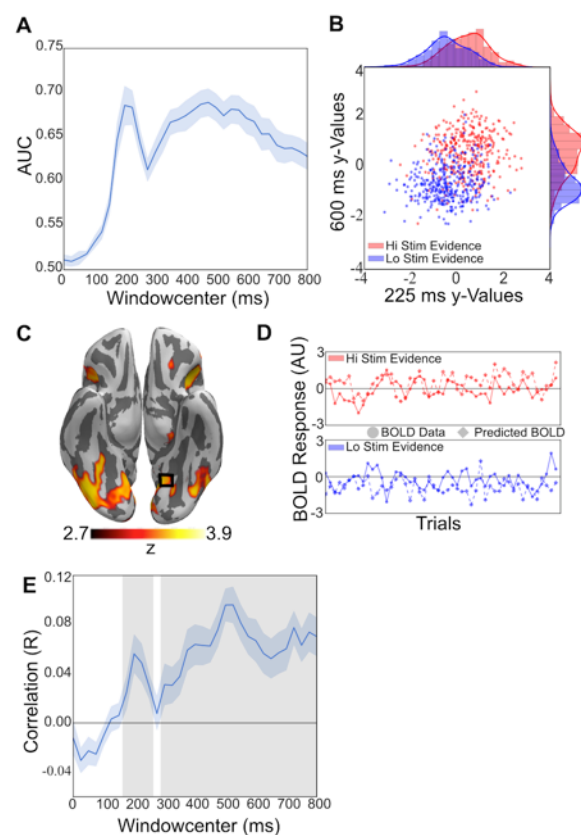


Figure 4.

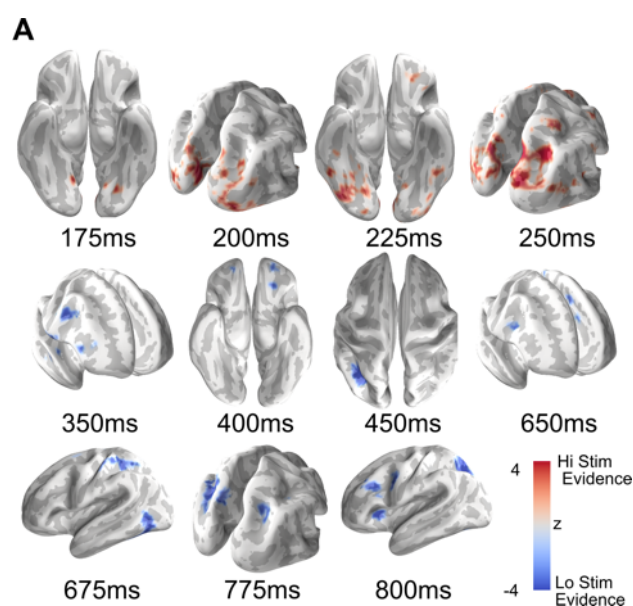


Figure 5.

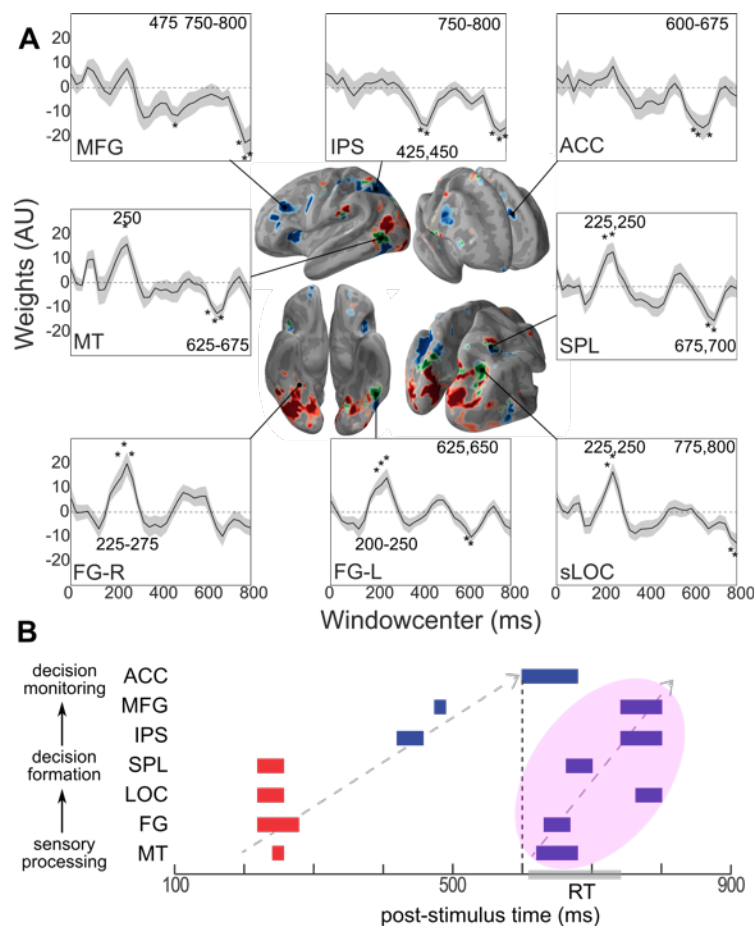


Figure 6.

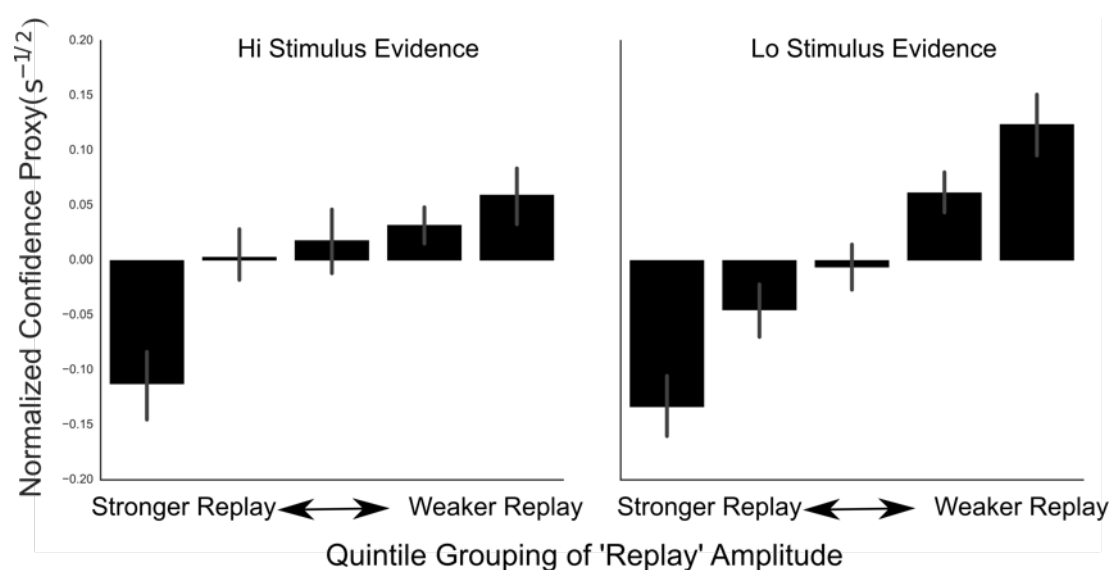


Figure 7.